Electronic Structure and Anisotropic Compression of Os_2B_3 to 358 GPa

Kaleb C. Burrage, Chia-Min Lin, Wei-Chih Chen, Cheng-Chien Chen*, and Yogesh K. Vohra*

Department of Physics, University of Alabama at Birmingham, Birmingham, AL, 35294, USA

E-mail: chencc@uab.edu; ykvohra@uab.edu

Abstract

High pressure study on ultra-hard transition-metal boride Os_2B_3 was carried out in a diamond anvil cell under isothermal and non-hydrostatic compression with platinum as an X-ray pressure standard. The ambient-pressure hexagonal phase of Os_2B_3 is found to be stable with a volume compression V/V_0 = 0.670 ± 0.009 at the maximum pressure of 358 ± 7 GPa. Anisotropic compression behavior is observed in Os_2B_3 to the highest pressure, with the *c*-axis being the least compressible. The measured equation of state using the 3rd-order Birch-Murnaghan fit reveals a bulk modulus K_0= 397 GPa and its first pressure derivative K_0'= 4.0. The experimental lattice parameters and bulk modulus at ambient conditions also agree well with our density-functional-theory (DFT) calculations within an error margin of ~1%. DFT results indicate that Os_2B_3 becomes more ductile under compression, with a strong anisotropy in the axial bulk modulus persisting to the highest pressure. DFT further enables the studies of charge distribution and electronic structure at high pressure. The pressure-enhanced electron density and repulsion along the *Os* and *B* bonds result in a high incompressibility along the crystal *c*-axis. Our work helps to elucidate the fundamental properties of Os_2B_3 under ultrahigh pressure for potential applications in extreme environments.

Keywords: transition-metal borides, ultra-hard materials, high pressure, diamond anvil cell, synchrotron x-ray diffraction, density functional theory, mechanical properties, crystal anisotropy

1. Introduction

The high-pressure behavior of ultra-hard and highly incompressible materials such as covalently bonded light elements (*C*, *N*, *O*, and *B*), refractory metals (*Re*, *Os*, etc.), and ceramic materials like transition-metal carbides and borides (*WC*, ReB_2, OsB_2, etc.) are of interest because of their superior mechanical properties and industrial applications as super abrasives [1-3]. The premium example of ultra-hard materials is diamond, and its mechanical and optical properties under extreme conditions have been studied in detail [4]. However, diamonds and other carbon-based materials are prone to oxidation in air at moderately high temperatures and reaction with ferrous alloys, which make them less desirable in many industrial applications. Transition-metal borides (TMBs) are proposed alternatives to diamond for abrasives and cutting tools, because some TMBs like OsB_2 have high hardness of 25-35 GPa [5-7] and thermal stability at high temperatures. The light-element boron forms covalent bonds with the transition metal once incorporated interstitially in the metal lattice. The directional covalent bonds combined with the high valence electron density gives the material its high incompressibility and hardness value. To date, micro-hardness at ambient pressure and high-pressure studies have been carried out on to a maximum pressures of 25-30 GPa, yet none has been conducted to pressures comparable to the bulk modulus of the material other than a static compression of ReB_2 to 241 GPa [8]. Gu et al. have showed that many TMBs, such as OsB_2, *OsB*, and Os_2B_3, have similar compression curves as diamond up to 30 GPa [9]. While many of the osmium-based TMBs were studied in detail, Os_2B_3 has received little attention. The boron atom positions and crystal structure within Os_2B_3 were not accurately determined until neutron diffraction experiments revealed its *B-B* distances in 2012 [10].

Recent advancements in diamond anvil cell (DAC) devices have allowed compression experiments to reach multi-megabar pressures using focused ion beam (FIB) machined diamond anvils [11-14]. These toroidal designs produced in Refs. [11] and [12] help reduce elastic deformation known as cupping in diamonds under extreme pressures. These developments have allowed diamond anvils to sustain static pressures as high as 5 megabars (500 GPa) in DACs, replicating pressures of inner-planetary cores [12]. In this study, we utilize the toroidal diamond anvil technology combined with X-ray diffraction (XRD) to compress the Os_2B_3 hexagonal phase. For the first time, ultra-incompressible Os_2B_3 is studied under static pressures up to 358 ± 7 GPa.

The experimental data show good agreements with corresponding first-principles simulations. This combined experiment-theory work provides insights to elucidate the fundamental properties of Os_2B_3 under ultrahigh pressure for extreme-environment applications.

2. Experimental and Computational Methods

Compression experiment on Os_2B_3 was carried out with specially fabricated diamond anvils that were machined using a Ga^+ focused ion beam (FIB). A toroidal design with a 16 micron culet and 40 micron outer region was made with a TESCAN LYRA 3 FIB parameters of 30keV accelerating voltage, 4.5 nA beam current, and a 50 nm beam size at the University of Alabama's Central Analytical Facility. The total depth of the toroid design was milled to 3 microns and was surrounded by an outer flat region extending to 60 microns shown in Figure 1. Two anvils were fabricated in this fashion and placed within a membrane driven diamond anvil cell (DAC) in an opposed anvil configuration. Compression of the sample material was conducted without using a pressure medium and was non-hydrostatic in nature. A rhenium gasket was indented to 25 micron thickness with a laser drilled sample hole of 8 micron diameter for sample placement. The gasket aids in the prevention of radial displacement of the sample material as well as minimizing diamond-diamond contact. The hexagonal phase of Os_2B_3 sample material (with space group $P6_3/mmc$) was bought from American Elements of purity 99.9% and mixed with platinum powder (99.97% purity) from Alfa-Aesar for pressure calibration.

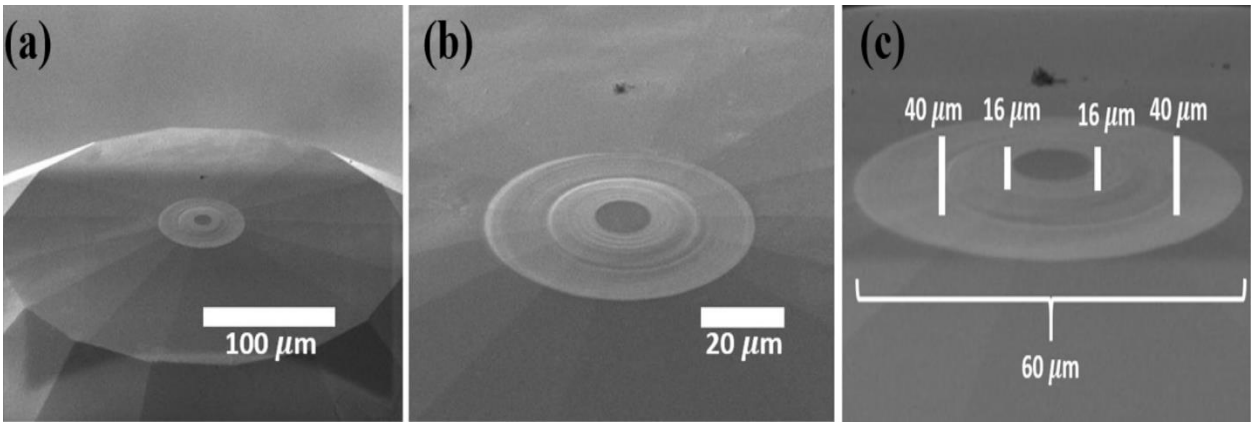

Figure 1. Top view of machined toroidal anvil atop beveled diamond anvil culet. (b) Close-up image of toroidal design on the central culet (c) Close-up side view of the toroidal anvil with design parameters of 16, 40, and 60 microns labeled.

X-ray diffraction (XRD) experiments were performed utilizing the X-ray diffraction setup at the HPCAT Beamline 16 BM-D at the Advanced Photon Source, Argonne National Laboratory [15]. The DAC was positioned so that an X-ray beam of wavelength $\lambda = 0.4133$ Å and beam size 3.7 μm (vertical) × 3.8 μm (horizontal) FWHM (full width half maximum) along the compression axis and incident on the sample. Pressure gradients across the beam width were not measured, however, they are expected to be minimal due to the small size of the x-ray beam (3-4 μm) compared to the diameter of the diamond culet (16 μm). XRD measurements were taken in approximately 2 GPa pressure steps totaling 157 data points. Scattered X-rays were collected on a Pilatus 1M detector situated downstream of beam incidence with sample to detector distance calibrated to 344.63 mm using CeO_2 calibration file analyzed in the Dioptas software. A schematic experimental setup was reported in Ref. [8]. The integrated sample XRD profiles were processed using the GSAS-II software [16] to extract crystal lattice parameters for the Os_2B_3 hexagonal phase, where the *Os* atom positions were held at (1/3, 2/3, 1/4) and the *B* atoms at (2/3, 1/3, 3/4). The Os_2B_3 data were fit to the 3rd-order Birch-Murnaghan equation of state (EOS) to determine the bulk modulus K_0 and its pressure derivative K_0' using the sample volumetric compression $x = V_0/V$:

$$P(V) = \frac{3}{2}K_0\left[x^{\frac{7}{3}} - x^{\frac{5}{3}}\right]\left[1 + \frac{3}{4}(K_0' - 4)\left(x^{\frac{2}{3}} - 1\right)\right]. \quad (1)$$

Ambient measurements of lattice parameters were taken at the University of Alabama at Birmingham via XRD analysis, and they were determined to be $a_0 = 2.915$ Å and $c_0 = 12.92$ Å for Os_2B_3. The ambient pressure platinum lattice parameter was also measured to be $a_0 = 3.924$ Å and LeBail refinement of platinum experimental XRD peaks showed error within pressure measurements to be under 2.0%.

The density functional theory (DFT) [17, 18] calculations were performed using a plane-wave basis and pseudopotential method as implemented in VASP (the Vienna ab initio simulation package, version 5.4.4) [19, 20]. We adopted the projector augmented wave (PAW) method [21, 22], and considered both the Ceperley–Alder–Perdew–Zunger local density approximation (LDA) functional [23] and the Perdew–Burke–Ernzerhof generalized gradient approximation (GGA) functional [24]. The *Os* $5d^6 6s^2$ and *B* $2s^2 2p^1$ states were treated as valence electrons, and a kinetic energy cutoff ENCUT of 420 eV was used in the expansion for the valence wave functions. Our

choice of ENCUT, which is 30% larger than the recommended value in the VASP pseudopotential files, suffices to converge the DFT total energy with a difference < 10^{-4} eV/atom. The Monkhorst–Pack sampling integration over the Brillouin zone [25] was chosen by a Γ-centered k-point mesh with a grid size of 31x31x7 (resolution = 0.01 × 2π/Å). The convergence criteria for self-consistent and structure relaxation calculations were set as 10^{-6} eV/unit cell and 10^{-3} eV/Å, respectively. The simulations are performed at zero temperature and various external pressures. At each given external pressure point, we first computed the fully relaxed lattice constants and atomic positions. Our calculated ambient lattice constants with the GGA functional are a_0 = 2.943 Å and c_0 = 12.939 Å, while those with the LDA functional are a_0 = 2.906 Å and c_0 = 12.814 Å. Both GGA and LDA results are similar to the experimental values, within an error margin of 1.0%.

After the structure relaxation, we then computed the elastic tensor by using the strain–stress method [26] as embedded in VASP. The calculations included contributions from distortions of rigid ions and ionic relaxations. The ionic contributions can be obtained by inverting the ionic Hessian matrix, which is the matrix of second energy derivatives with respect to atomic positions, and multiplied by the internal strain tensor [27]. Base on the stress–strain relationship, we can derive the elastic constants C_{ij} and determine various mechanical properties. For example, in the Vogit–Reuss–Hill approximations [28-30], the bulk modulus (K) and shear modulus (G) are obtained as follows:

$$K = (K_V + K_R)/2 \quad , G = (G_V + G_R)/2, \tag{2}$$

$$K_V = [(C_{11} + C_{22} + C_{33}) + 2(C_{12} + C_{13} + C_{23})]/9, \tag{3}$$

$$K_R = 1/[S_{11} + S_{22} + S_{33} + 2(S_{12} + S_{23} + S_{31})], \tag{4}$$

$$G_V = [(C_{11} + C_{22} + C_{33}) - 2(C_{12} + C_{23} + C_{31}) + 3(C_{44} + C_{55} + C_{66})]/15, \tag{5}$$

$$G_R = 15/[4(S_{11} + S_{22} + S_{33}) - 4(S_{12} + S_{23} + S_{31}) + 3(S_{44} + S_{55} + S_{66})]. \tag{6}$$

Here, C_{ij} and S_{ij} are elastic constants and elastic compliances, respectively. The computed bulk modulus values K_0 at ambient conditions are 358.9 GPa with GGA, and 391.7 GPa with LDA. The LDA bulk modulus is consistent with previous theoretical values [9, 31], and it also agrees better (within an error margin of 1.5%) with the experimental value K_0 = 397 GPa obtained by fitting the experimental P-V curve to equation (1). In our GGA and LDA calculations of the mechanical

properties, their overall trends with pressure are comparable. Since the results from the LDA functional agree better with the corresponding experiments, below we will mainly present and discuss the LDA results. Finally, the theoretical structural visualization and charge distribution were plotted by the VESTA software (version 3.4.8) [32].

3. Results

Figure 2 shows the integrated XRD pattern with Lebail fit to the XRD data at the maximum pressure of 358 ± 7 GPa. The dotted curve shown below the XRD peaks is the difference curve between the sample data and the Lebail fit to the data. Strong Os_2B_3 *hkl* peaks are labeled and coexist with weaker OsB_2 impurity peaks labeled with asterisks. Platinum peaks used for pressure calibration are labeled in red in Figure 2.

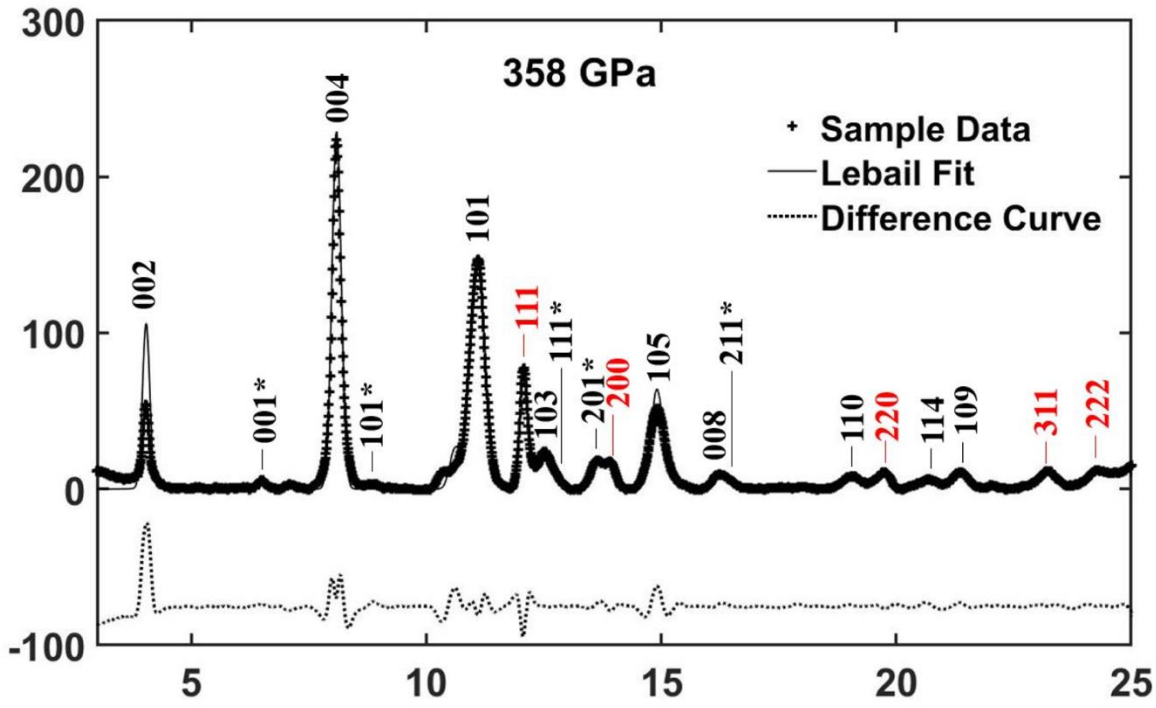

Figure 2. Integrated x-ray diffraction profile along with Lebail fit for the weak orthorhombic OsB_2 (marked by an asterisk) and the hexagonal Os_2B_3 phases at the highest pressure of 358 ± 7.04 GPa. The platinum pressure marker peaks are indicated in red. The dotted curve at the bottom is the difference curve between the observed intensities and the Lebail fit.

Figure 3(a) displays the relative axial compression of lattice parameters for the hexagonal phase of Os_2B_3. The lattice *a* parameter was shown to be the most compressible, while the lattice

c parameter is the least compressible, with the values of $a = 2.507 \pm 0.004$ Å and $c = 11.71 \pm 0.021$ Å at the maximum pressure. It is to be noted that the anisotropy between compression of the *a*-axis and *c*-axis increases with pressure to the highest pressure of 358 ± 7 GPa. The non-hydrostatic component of pressure may impact the observed anisotropy at low pressures, however, at higher pressures when pressure is much greater than the shear strength of material we expect these effects to be minimal. The effects of anisotropy also can be seen in the compression ratio of *c* and *a* lattice parameters in Figure 4. The *a*-axis is compressed more rapidly, resulting in an increasing *c/a* ratio to the maximum value of $c/a = 4.672 \pm 0.008$. The ratio begins to flatten out with higher pressure as the axes are compressed more equally. Due to enhanced interatomic interactions with increasing pressure, the material becomes stiffer. At higher enough pressure, the *a* and *c* lattice parameters will eventually tend to saturate and become weakly pressure-dependent, resulting in a slower increase of the *c/a* ratio. Figure 3(b) is the corresponding volumetric compression data fitted with the 3rd-order Birch-Murnaghan EOS. No phase change was observed, and the hexagonal Os_2B_3 phase remained stable to 358 GPa, with a maximum volume compression $V/V_0 = 0.670 \pm 0.009$. As mentioned above, the ambient bulk modulus K_0=397 GPa and pressure derivative K_0'= 4.0 were obtained by fitting with equation (1).

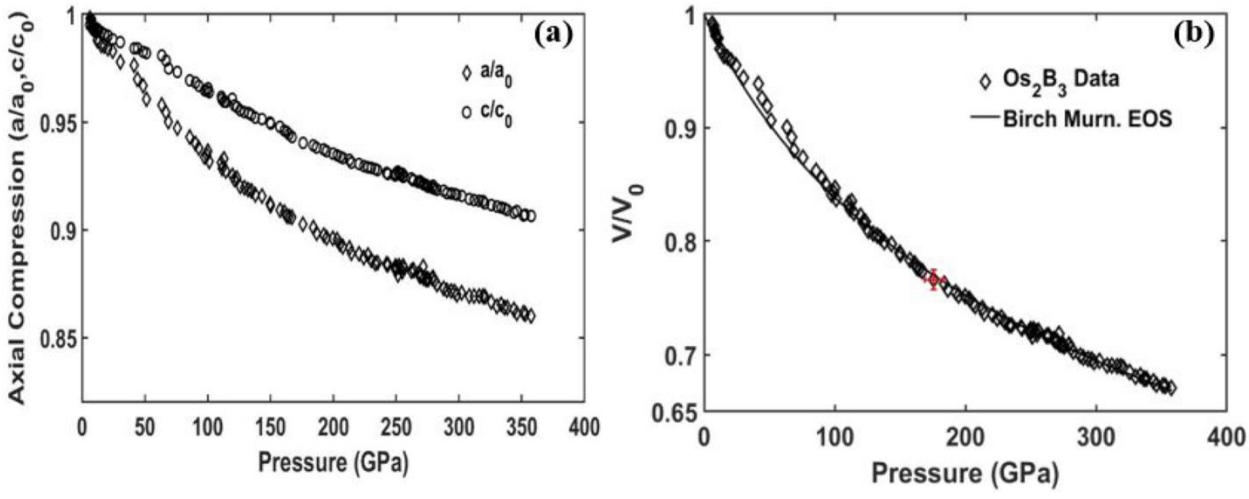

Figure 3. (a) Axial compression of Os_2B_3 as a function of pressure up to 358 ± 7.04 GPa. (b) Volumetric compression of Os_2B_3 fitted to the 3rd-Order Birch Murnaghan equation of state. Sample compression remains stable and no phase change was observed.

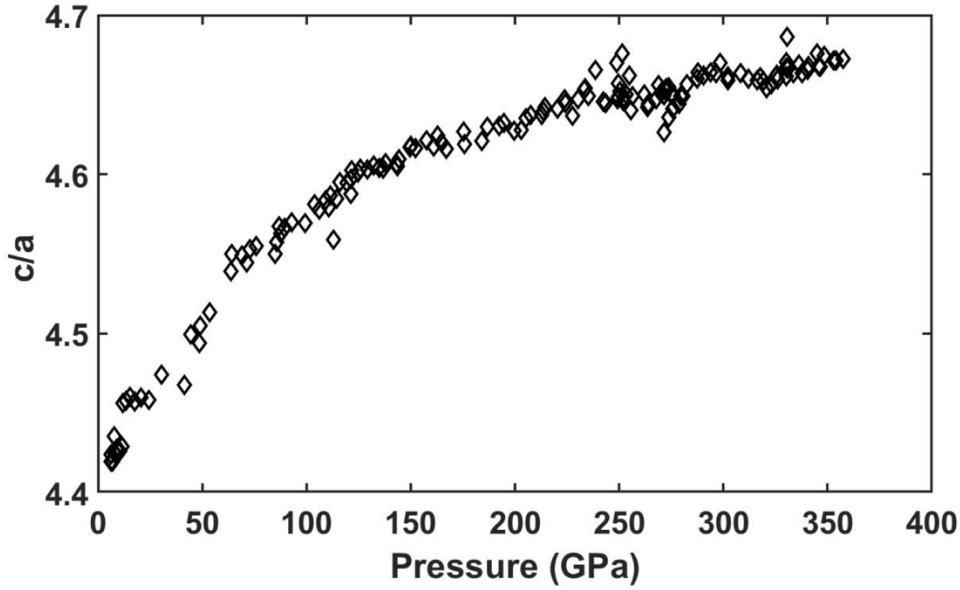

Figure 4. Compression ratio of the lattice *c* and *a* parameters as a function of pressure up to 358 ± 7 GPa. The *c/a* ratio is seen to increase and flatten with increasing pressure.

Figure 5 shows our DFT calculations of lattice parameters with the LDA functional for hexagonal Os_2B_3 under hydrostatic compression up to 360 GPa. The DFT-LDA ambient lattice parameters a_0 = 2.906 Å and c_0 = 12.814 Å are within an error margin of 1% compared to the experiments. At the highest pressure of 360 GPa, the DFT-LDA value of a/a_0 = 0.852 slightly underestimates the experimental value of 0.860, while the DFT-LDA value of c/c_0 = 0.916 slightly overestimates the experimental value of 0.906. On the other hand, the DFT-LDA value of V/V_0 = 0.664 agree well with the experimental value of 0.670 at maximum compression. As mentioned in the previous section, the computed DFT-LDA bulk modulus value of K_0 = 391.7 GPa also matches well with the experimental fitted value of K_0 = 397 GPa. Therefore, for hexagonal Os_2B_3, DFT calculations utilizing the LDA functional have led to good theory-experiment agreements. We note that our theoretical volume versus pressure curve is a concave up function, which suggests that the curve protrusion observed experimentally between the pressure range 40 – 70 GPa in Figure 3 is potentially caused by a non-hydrostatic condition. The theoretical results also indicated a distinct anisotropic behavior, with the *c*-axis being more incompressible than the *a*-axis. Below we will discuss the anisotropic behavior in more detail by further examining the electronic structures and pressure evolutions of elastic constants.

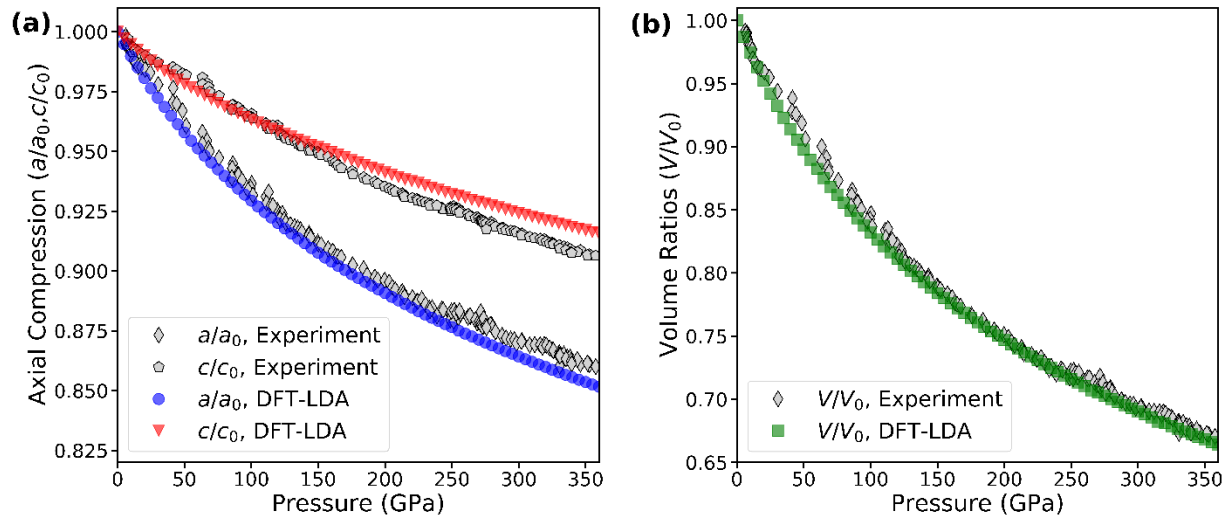

Figure 5. (a) Theoretical hydrostatic pressure dependence of the axial compression for lattice parameters a/a_0 and c/c_0 up to 360 GPa for hexagonal Os_2B_3. The density functional theory (DFT) calculations were performed with the local density approximation (LDA) functional. (b) Corresponding ratio of unit-cell volume V/V_0 versus pressure curve. The experimental values are plotted accordingly.

4. Discussion

Figure 6 shows the Os_2B_3 hexagonal structures (with space group $P6_3/mmc$) and iso-surfaces of charge density under different external pressures. The crystal structure of Os_2B_3 can be depicted as stackings of *Os* and *B* layers along the *c*-direction. The *B*-*B* bond length is near 1.9 Å. There is an offset between the *B* and *Os* atoms in the *a*-axis, suggesting that their electrostatic repulsive forces do not directly push each other. On the other hand, the *B* and *Os* atoms are directly aligned along the *c*-axis, which leads to highly oriented repulsive electron–electron interactions. When the applied pressure increases, in addition to *B*-*B* covalent bonds, a substantial amount of electron density is centered along the *Os*-*B* bond direction, indicating strong directional bonding behavior along the *c*-axis. Since materials with a large hardness are likely to have highly directional bonds [7, 8, 33], our theoretical results suggest that the highest hardness of Os_2B_3 should occur along the *c*-axis.

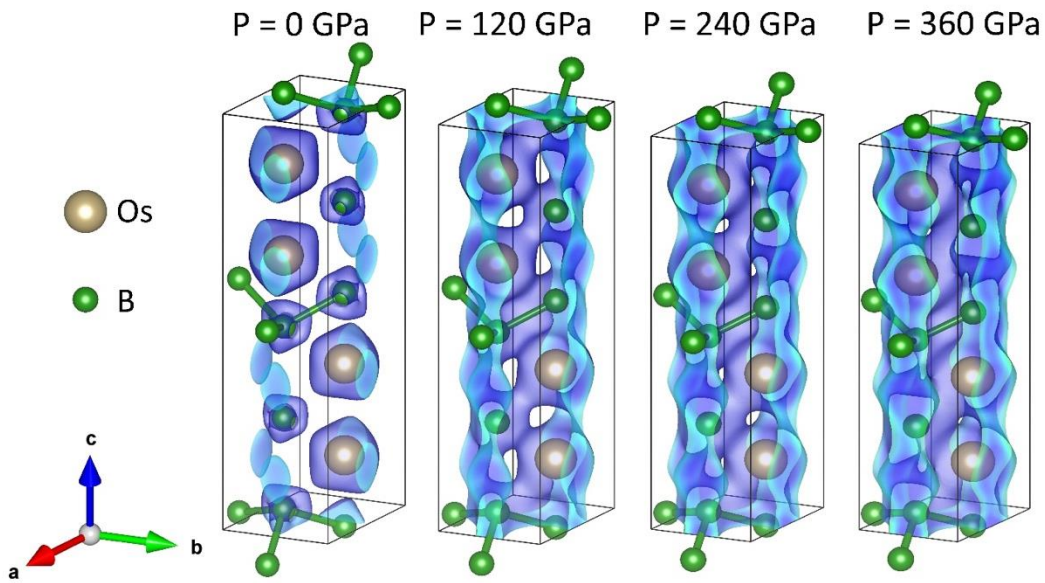

Figure 6. Os_2B_3 hexagonal crystal structures and iso-surfaces of charge density at different pressures. The iso-surface levels were set to be 0.1 a_0^{-3} (with a_0 being the Bohr radius). The input data for the VESTA plotting software are based on the VASP output file CHGCAR, which contains the lattice vectors, atomic coordinates, the total charge density multiplied by the volume on the fine fast Fourier transform-grid, and the projector augmented wave one-center occupancies.

In addition to charge density, we have studied the electronic density of states (DOS) of Os_2B_3. Figure 7 shows the computed DOS at 0 GPa (top) and 360 GPa (bottom), respectively. We have adjusted the Wigner-Seitz radius for each atom type at different pressure point, in order to reduce the overlap between atomic spheres when integrating the DOS. At 0 GPa, the DOS has a predominant *Os* character at the Fermi level (E_F). At high pressure, the partial DOS at E_F from *Os* and *B* atoms both increase, implying that metallic bonding is increased or covalent bonding is reduced. The behavior is consistent with the iso-surface charge density plot in Figure 6 and the pressure-enhanced ductility to be discussed later in Figure 9. On the other hand, pressure also causes a stronger hybridization between *Os* and *B* atoms, as well as between *B* atoms themselves. Therefore, strong covalent *Os*-*B* and *B*-*B* bonds are still present. The strong *Os*-*B* bonding is also responsible for the *c*-axis incompressibility of Os_2B_3 at high pressure.

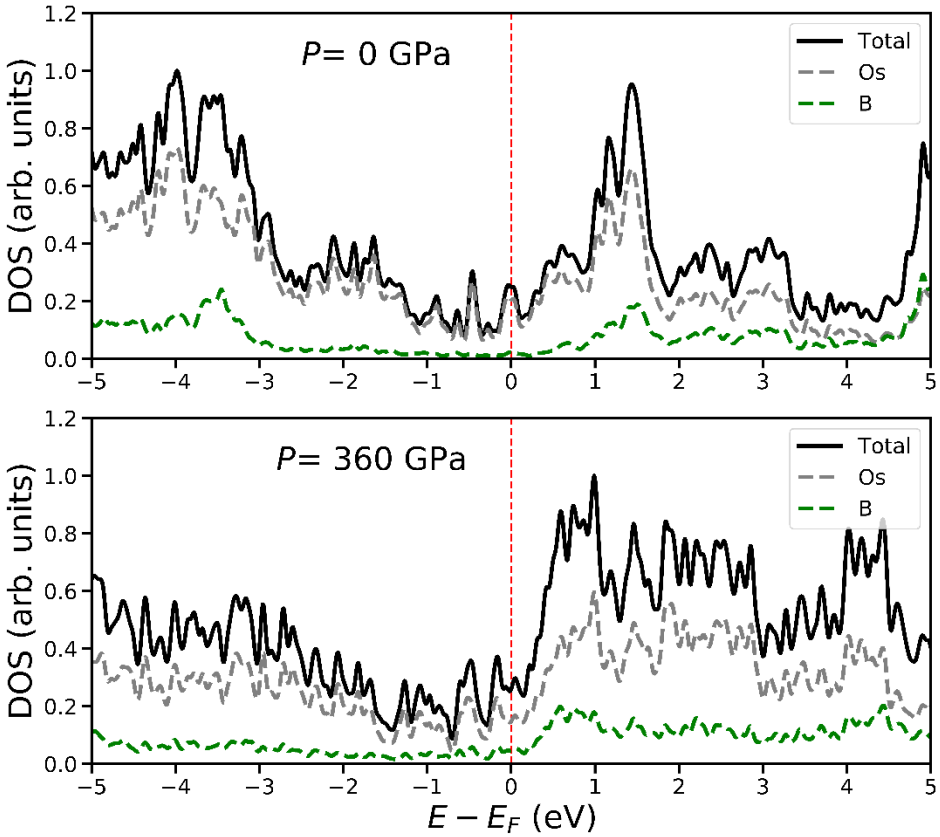

228

229 **Figure 7.** Theoretical Os_2B_3 density of states (DOS) calculated by density functional theory (DFT) using
230 the local density approximation (LDA) functional at pressure P = 0 GPa (top) and P = 360 GPa (bottom).
231 The vertical dashed line indicates the Fermi level (E_F).

232 To further study the mechanical properties, we resort to the elastic constants C_{ij} obtained
233 directly in our DFT calculations. Due to the hexagonal symmetry of Os_2B_3 (with a space group
234 $P6_3/mmc$), there are only five independent elastic coefficients: C_{11}, C_{12}, C_{13}, C_{33}, C_{44}. These five
235 elastic coefficients together with $C_{66} = (C_{11}-C_{12})/2$ are shown in Figure 8(a). C_{11} and C_{33} represent
236 resistances to compression along the *a*-axis and *c*-axis, respectively. It is noted that C_{11} and C_{33} are
237 largely increased under pressure, indicating a strong incompressibility along both axes.
238 Furthermore, C_{33} is larger than C_{11}, which suggests that the *c*-axis is the least compressible. As
239 discussed before, this strong *c*-axis incompressibility is related to the strong electron charge
240 density and repulsion in the *Os-B* bonds along the *c*-direction. C_{44} and C_{66} are the parameters that
241 directly determine the indentation hardness of a solid [34]. The large C_{44} and C_{66} indicate a strong
242 resistance to uniaxial shear strain in the (100) and (001) planes, respectively. Here, $C_{66} < C_{44}$, hence
243 shear distortion along the (100) plan is more difficult. Moreover, C_{11} and C_{33} are higher than C_{44}

and C_{66}, which indicate that unidirectional compression resistances along the main crystal axes are higher than the shear deformation resistances.

We next consider the axial bulk moduli along the *a*-axis (B_a) and *c*-axis (B_c) [35] to describe the anisotropic elasticity of Os_2B_3:

$$B_a = \alpha/(2+\beta) \quad , B_c = B_a/\beta, \tag{7}$$

$$\alpha = 2(C_{11}+C_{12}) + 4C_{13}\alpha + C_{33}\alpha^2, \tag{8}$$

$$\beta = (C_{11}+C_{12}-2C_{13})/(C_{33}-C_{13}). \tag{9}$$

The pressure evolutions of B_a and B_c are given in Figure 8(b). It is noted that B_c is always larger than B_a in the pressure range under study, suggesting a strong anisotropy of the elasticity in the hexagonal phase of Os_2B_3. This result is consistent with the behaviors of C_{11} and C_{33} as a function of pressure, showing that compression along the *c*-axis is more difficult.

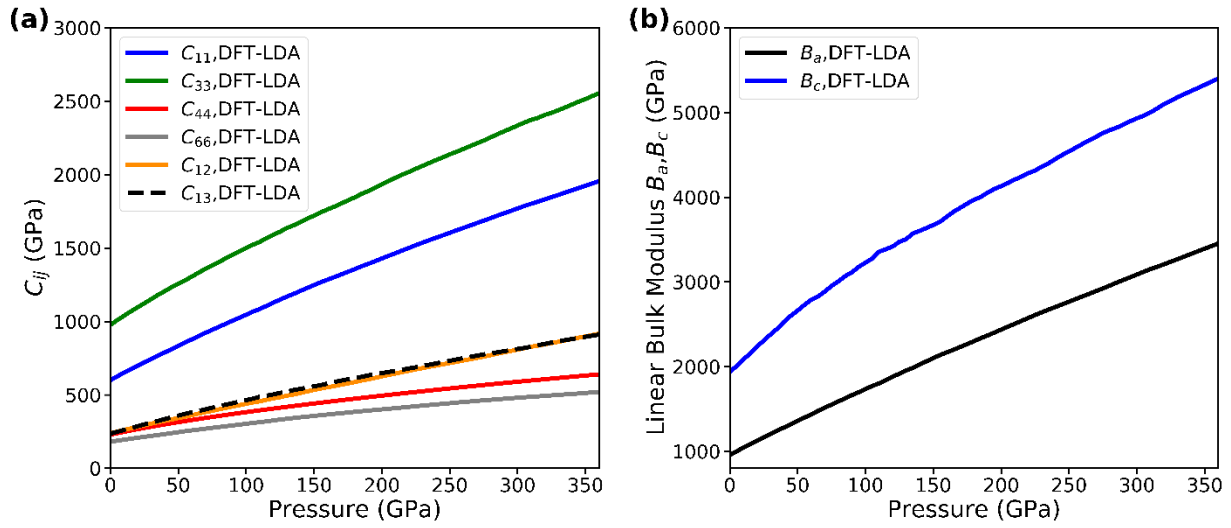

Figure 8. (a) Selected elastic constants versus pressure for hexagonal Os_2B_3. The density functional theory (DFT) calculations were performed with the local density approximation (LDA) functional. (b) Axial bulk moduli (defined in the main text) along the *a*-axis (B_a) and *c*-axis (B_c) as a function of pressure. The calculations were based on the elastic constants in (a).

Finally, it is noted that the shear modulus (G) and bulk modulus (K) can help predict a material's brittle or ductile behavior, which is related to its reversible compressive deformation and fracture ability. In particular, according Pugh's criterion [36], a material behaves in a ductile

manner if $G/K < 0.571$, or otherwise it should be brittle in nature. Figure 9(a) shows the calculated values of G and K as a function of pressure. While both G and K are increased by compression, K grows faster than G. This indicates that G/K is decreased with pressure, as shown in Figure 9(b). The computed G/K ratio at 0 GPa is 0.564, and at 360 GPa is 0.457. Since a low (high) G/K value is associate with ductility (brittleness), the ductile behavior of Os_2B_3 is enhanced with pressure. Poisson's ratio is another good indicator of the brittle or ductile behavior, and it can be obtained by $(3K - 2G)/[2(3K + G)]$. According to Frantsevich's rule [37], a material with a larger Poisson's ratio (>1/3) is ductile, or otherwise it is brittle. Figure 9(b) shows that the Poisson's ratio of Os_2B_3 is increased under compression, again implying a pressure-enhanced ductility.

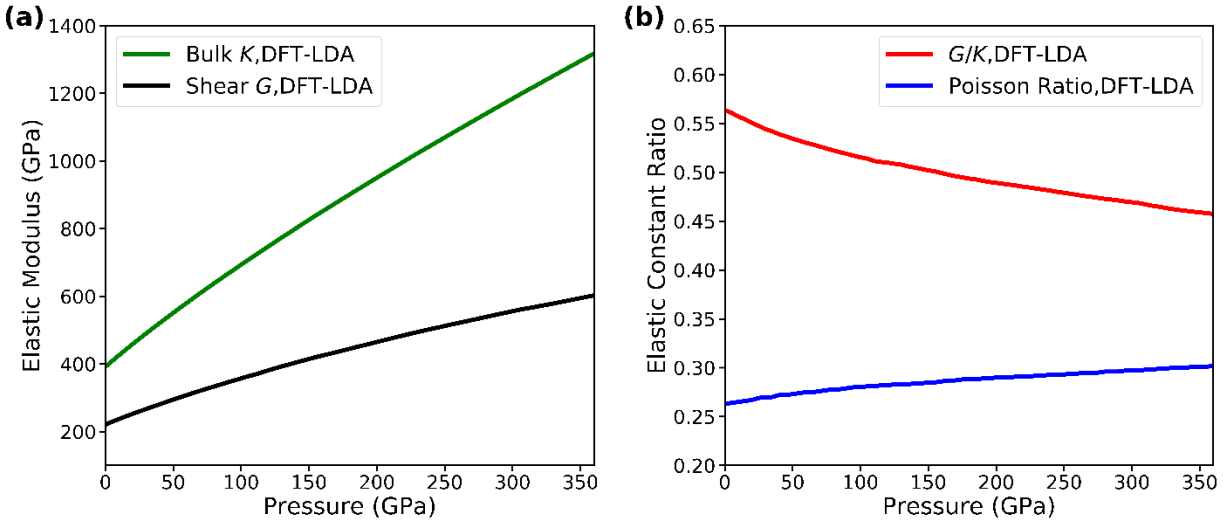

Figure 9. (a) Theoretical bulk (K) and shear (G) moduli of Os_2B_3 as a function of pressure. The density functional theory (DFT) calculations were performed with the local density approximation (LDA) functional. G and K were obtained by using the Voigt–Reuss–Hill approximation [Equations (2) – (6)] and the DFT-LDA elastic constants. (b) The G/K and Poisson ratios as a function of pressure.

The study on transition-metal boride under high pressure can offer unique insights in the changes in electronic structure induced by compression. Three dimensional covalent sp^3 bonds of carbon atoms gives diamond its ultra-hardness and incompressibility, indicating the necessary role of covalent bonds if one wishes to replicate diamond's supreme physical properties. As discussed above, the pressure-enhanced *Os-B* covalent bonds in Os_2B_3 can cause a strong resistance to compression and a highly anisotropic behavior. Although the bulk modulus value of Os_2B_3 is shown to be comparable to that of diamond, this alone does not necessarily guarantee a high strength, as the latter corresponds to resistance to plastic deformation. There are also *Os-Os*

metallic bonds that would indicate weak resistance to deformation along certain axis. In addition, Os_2B_3 has a similar hexagonal structure to ReB_2 but differs by having alternating planar boron layers with puckered boron layers [8]. This puckering of boron atoms may act as a potential shield to atomic dislocation under applied loads. Ref. [9] has shown a micro-hardness value of 15 GPa for Os_2B_3, which is thereby not a super-hard material. However, this does not rule out practical mechanical applications to utilize Os_2B_3 or other transition metal borides, because of their impressive bulk modulus values and stability at high temperatures.

5. Conclusion

Isothermal and non-hydrostatic compression experiments utilizing toroidal diamond anvil cell technology has allowed for the first-time a unique look at Os_2B_3 under pressure conditions replicating planetary interiors, with a maximum volume compression value of $V/V_0 = 0.670 \pm 0.009$ for Os_2B_3 at 358 ± 7.04 GPa. Increasing anisotropy between the lattice c and a parameters was also shown to persist to the highest pressure. Bulk modulus and its first pressure derivatives were calculated from a fit to the 3rd-order Birch Murnaghan equation of state for Os_2B_3, with K_0=397 GPa and K_0'= 4.0, which are comparable to the values in other ultra-hard materials. The results from density functional theory simulations were in good agreement with the experiments. The high bulk modulus, anisotropic behavior, and ultra-incompressible features of Os_2B_3 thereby make it a potential material for extreme-environment applications.

Acknowledgments

This research is funded by the U.S. National Science Foundation under Metals and Metallic Nanostructures Program Grant No. DMR-1904164. Any opinions, findings, and conclusions or recommendations expressed in this material are those of the authors and do not necessarily reflect the views of the National Science Foundation. Portions of this work were performed at HPCAT (Sector 16), Advanced Photon Source (APS), Argonne National Laboratory. HPCAT operations are supported by DOE-NNSA's Office of Experimental Sciences. The Advanced Photon Source is a U.S. Department of Energy (DOE) Office of Science User Facility operated for the DOE Office of Science by Argonne National Laboratory under Contract No. DE-AC02-06CH11357. The calculations were performed on the Frontera computing system at the Texas Advanced Computing Center. Frontera is made possible by National Science Foundation award OAC-1818253.

References

1. Friedrich, A., et al., *Synthesis of Binary Transition Metal Nitrides, Carbides and Borides from the Elements in the Laser-Heated Diamond Anvil Cell and Their Structure-Property Relations.* Materials, 2011. **4**: p. 1648-1692.
2. Yeung, M.T., R. Mohammadi, and R.B. Kaner, *Ultraincompressible, Superhard Materials.* Annu. Rev. Mater. Res., 2016. **46**: p. 465-485.
3. Kvashnin, A.G., Z. Allahyari, and A.R. Oganov, *Computational discovery of hard and superhard materials.* J. Appl. Phys., 2019. **126**: p. 040901.
4. Aleksandrov, I., et al., *Diamond at high pressures: Raman scattering of light, equation of state, and high pressure scale.* Zh. Eksp. Teor. Fiz, 1987. **93**: p. 680-691.
5. Cumberland, R.W., et al., *Osmium diboride, an ultra-incompressible, hard material.* Journal of the American Chemical Society, 2005. **127**(20): p. 7264-7265.
6. Hebbache, M., L. Stuparević, and D. Živković, *A new superhard material: Osmium diboride OsB2.* Solid state communications, 2006. **139**(5): p. 227-231.
7. Kaner, R.B., J.J. Gilman, and S.H. Tolbert, *Designing superhard materials.* Science, 2005. **308**(5726): p. 1268-1269.
8. Burrage, K.C., et al., *Experimental and Computational Studies on Superhard Material Rhenium Diboride under Ultrahigh Pressures.* Materials, 2020. **13**(7): p. 1657.
9. Gu, Q., G. Krauss, and W. Steurer, *Transition metal borides: superhard versus ultra-incompressible.* Advanced materials, 2008. **20**(19): p. 3620-3626.
10. Frotscher, M., A. Senyshyn, and B. Albert, *Neutron diffraction at metal borides, Ru2B3 and Os2B3.* Zeitschrift für anorganische und allgemeine Chemie, 2012. **638**(12-13): p. 2078-2080.
11. Dewaele, A., et al., *Toroidal diamond anvil cell for detailed measurements under extreme static pressures.* Nature communications, 2018. **9**(1): p. 1-9.
12. Jenei, Z., et al., *Single crystal toroidal diamond anvils for high pressure experiments beyond 5 megabar.* Nature communications, 2018. **9**(1): p. 1-6.
13. Sakai, T., et al., *High pressure generation using double-stage diamond anvil technique: problems and equations of state of rhenium.* High Pressure Research, 2018. **38**(2): p. 107-119.
14. Sakai, T., et al., *High-pressure generation using double stage micro-paired diamond anvils shaped by focused ion beam.* Review of Scientific Instruments, 2015. **86**(3): p. 033905.
15. Park, C., et al., *New developments in micro-X-ray diffraction and X-ray absorption spectroscopy for high-pressure research at 16-BM-D at the Advanced Photon Source.* Review of Scientific Instruments, 2015. **86**(7): p. 072205.
16. Toby, B.H. and R.B. Von Dreele, *GSAS-II: the genesis of a modern open-source all purpose crystallography software package.* Journal of Applied Crystallography, 2013. **46**: p. 544-549.
17. Hohenberg, P. and W. Kohn, *Density functional theory (DFT).* Phys. Rev, 1964. **136**: p. B864.
18. Kohn, W. and L.J. Sham, *Self-consistent equations including exchange and correlation effects.* Physical review, 1965. **140**(4A): p. A1133.
19. Kresse, G. and J. Furthmüller, *Efficiency of ab-initio total energy calculations for metals and semiconductors using a plane-wave basis set.* Computational materials science, 1996. **6**(1): p. 15-50.

20. Kresse, G. and J. Furthmüller, *"Efficient iterative schemes for ab initio total-energy calculations using a plane-wave basis set," Phys. Rev. B, vol. 54, pp. 11169-11186.* 1996.

21. Blöchl, P.E., *Projector augmented-wave method.* Physical review B, 1994. **50**(24): p. 17953.

22. Kresse, G. and D. Joubert, *From ultrasoft pseudopotentials to the projector augmented-wave method.* Physical review b, 1999. **59**(3): p. 1758.

23. Ceperley, D.M. and B.J. Alder, *Ground state of the electron gas by a stochastic method.* Physical review letters, 1980. **45**(7): p. 566.

24. Perdew, J.P., K. Burke, and M. Ernzerhof, *Generalized gradient approximation made simple.* Physical review letters, 1996. **77**(18): p. 3865.

25. Monkhorst, H.J. and J.D. Pack, *Special points for Brillouin-zone integrations.* Physical review B, 1976. **13**(12): p. 5188.

26. Le Page, Y. and P. Saxe, *Symmetry-general least-squares extraction of elastic data for strained materials from ab initio calculations of stress.* Physical Review B, 2002. **65**(10): p. 104104.

27. Wu, X., D. Vanderbilt, and D. Hamann, *Systematic treatment of displacements, strains, and electric fields in density-functional perturbation theory.* Physical Review B, 2005. **72**(3): p. 035105.

28. Hill, R., *The elastic behaviour of a crystalline aggregate.* Proceedings of the Physical Society. Section A, 1952. **65**(5): p. 349.

29. Reuß, A., *Berechnung der fließgrenze von mischkristallen auf grund der plastizitätsbedingung für einkristalle.* ZAMM-Journal of Applied Mathematics and Mechanics/Zeitschrift für Angewandte Mathematik und Mechanik, 1929. **9**(1): p. 49-58.

30. Voigt, W., *Lehrbuch der kristallphysik*. Vol. 962. 1928: Teubner Leipzig.

31. Ozisik, H., et al., *Anisotropic elastic and vibrational properties of Ru2B3 and Os2B3: a first-principles investigation.* Materials Research Express, 2016. **3**(7): p. 076501.

32. Momma, K. and F. Izumi, *VESTA 3 for three-dimensional visualization of crystal, volumetric and morphology data.* Journal of applied crystallography, 2011. **44**(6): p. 1272-1276.

33. Chung, H.-Y., et al., *Synthesis of ultra-incompressible superhard rhenium diboride at ambient pressure.* Science, 2007. **316**(5823): p. 436-439.

34. Connétable, D. and O. Thomas, *First-principles study of the structural, electronic, vibrational, and elastic properties of orthorhombic NiSi.* Physical review B, 2009. **79**(9): p. 094101.

35. Islam, A., A. Sikder, and F. Islam, *NbB2: a density functional study.* Physics Letters A, 2006. **350**(3-4): p. 288-292.

36. Pugh, S., *XCII. Relations between the elastic moduli and the plastic properties of polycrystalline pure metals.* The London, Edinburgh, and Dublin Philosophical Magazine and Journal of Science, 1954. **45**(367): p. 823-843.

37. Frantsevich, I.N., ed. *Elastic Constants and Elastic Moduli of Metals and Insulators Handbook*. 1983, Naukova Dumka: Kiev, Ukraine.